Propagation of Errors from the Sensitivity Image in List Mode Reconstruction

Jinyi Qi, *Member, IEEE,* and Ronald H Huesman, *Fellow, IEEE*

Abstract—**List mode image reconstruction is attracting renewed attention. It eliminates the storage of empty sinogram bins. However, a single back projection of all LORs is still necessary for the pre-calculation of a sensitivity image. Since the detection sensitivity is dependent on the object attenuation and detector efficiency, it must be computed for each study. Exact computation of the sensitivity image can be a daunting task for modern scanners with huge numbers of LORs. Thus, some fast approximate calculation may be desirable. In this paper, we theoretically analyze the error propagation from the sensitivity image into the reconstructed image. The theoretical analysis is based on the fixed point condition of the list mode reconstruction. The non-negativity constraint is modeled using the Kuhn-Tucker condition. With certain assumptions and the first order Taylor series approximation, we derive a closed form expression for the error in the reconstructed image as a function of the error in the sensitivity image. The result provides insights on what kind of error might be allowable in the sensitivity image. Computer simulations show that the theoretical results are in good agreement with the measured results.**

I. Introduction

List mode image reconstruction has recently attracted renewed attention as the number of possible lines of response (LORs) in modern scanners becomes more than the number of detected events in one data set [1], [2], [3], [4], [5], [6]. One advantage is that it eliminates the storage of empty sinogram bins. The likelihood function of list mode data can be written as [2]

$$L(\boldsymbol{x}) = \sum_{k=1}^{K} \log \sum_{j=1}^{N} p(i_k, j) x_j - \sum_{j=1}^{N} \varepsilon_j x_j, \tag{1}$$

where x_j is the mean activity inside the jth voxel of the unknown image, $p(i,j)$ is the probability of detecting an event from the jth voxel in the ith LOR, i_k is the index of the LOR of the kth detection, $\varepsilon_j \equiv \sum_i p(i,j)$ is the sensitivity image, K is the total number of detections, and N is the total number of image voxels.

Irrespective of the data format, when the statistical properties of the data are modeled as Poisson, forward and back projection need not be calculated for unrepresented LORs during iterative reconstruction. However, a single back projection of all LORs is still necessary for the pre-calculation of the sensitivity image ε_j. Since $p(i,j)$ includes object attenuation and detector efficiency, ε_j needs to be computed for each study. For systems with huge numbers of LORs (e.g., [2], [7]) or imaging with subject motion (e.g., [8], [9]), exact computation of ε_j may require more time than reconstruction itself.

One remedy to this problem is to use some fast approximate methods in the computation of the sensitivity image. For example, Carson *et al* [9] proposed to calculate the sensitivity image by backprojecting randomly sampled LORs. Inevitably, errors will be introduced to the sensitivity image. In this paper, we study the impact of the such errors on the final reconstructed images.

II. Theory

While an ML estimate can be obtained by maximizing (1), ML solutions are very noisy because emission tomography is an ill-posed problem. Thus, some form of regularization (or prior function) is needed to reconstruct a reasonable image.

Bayesian methods regularize the image through the use of a prior distribution on the unknown image. Most image priors have a Gibbs distribution of the form

$$p(\boldsymbol{x}) = \frac{1}{Z} e^{-\beta U(\boldsymbol{x})}, \tag{2}$$

where $U(\boldsymbol{x})$ is the energy function, β is the smoothing parameter that controls the resolution of the reconstructed image, and Z is a normalization constant. For quadratic priors, the energy function can be expressed as

$$U(\boldsymbol{x}) = \frac{1}{2}\, \boldsymbol{x}' \boldsymbol{R} \boldsymbol{x}, \tag{3}$$

where $\boldsymbol{R}$ is a positive definite (or semidefinite) matrix and $'$ denotes transpose.

Combining the likelihood function and the image prior, the MAP reconstruction is found as

$$\hat{\boldsymbol{x}} = \arg\max_{\boldsymbol{x} \geq 0} \left[L(\boldsymbol{x}) - \beta U(\boldsymbol{x}) \right]. \tag{4}$$

Since $L(\boldsymbol{y}|\boldsymbol{x})$ is a concave function of $\boldsymbol{x}$, (4) generally has a unique solution for convex priors. The necessary and sufficient condition for $\hat{\boldsymbol{x}}$ to be the solution of (4) is the Kuhn-Tucker condition [10]

$$\sum_k \frac{p(i_k,j)}{\sum_l p(i_k,l)\hat{x}_l} - \varepsilon_j - \beta \frac{\partial}{\partial x_j} U(\hat{\boldsymbol{x}}) \begin{cases} = 0, \ \hat{x}_j > 0 \\ \leq 0, \ \hat{x}_j = 0 \end{cases} \qquad j = 1, \ldots, N. \tag{5}$$

Let us denote the approximated sensitivity image by $\boldsymbol{\varepsilon}^* = \boldsymbol{\varepsilon} + \delta\boldsymbol{\varepsilon}$. The reconstructed image with the approximated sensitivity image, $\hat{\boldsymbol{x}}^*$, satisfies

$$\sum_k \frac{p(i_k,j)}{\sum_l p(i_k,l)\hat{x}^*_l} - \varepsilon_j - \delta\varepsilon_j - \beta \frac{\partial}{\partial x_j} U(\hat{\boldsymbol{x}}^*) \begin{cases} = 0, \ \hat{x}^*_j > 0 \\ \leq 0, \ \hat{x}^*_j = 0 \end{cases} \tag{6}$$

This work is supported in part by the Director, Office of Science, Office of Biological and Environmental Research, Medical Sciences Division, of the U.S. Department of Energy under contract no. DE-AC03-76SF00098, and by the National Institutes of Health under grant nos. R01 CA67911, R01 EB00194.

The authors are with the Department of Nuclear Medicine and Functional Imaging, Lawrence Berkeley National Laboratory, Berkeley, CA 94720, USA (telephone: 510-486-4695, e-mail: jqi@lbl.gov)

Since the gradient at the voxel $\hat{x}_j = 0$ is almost always negative and a small perturbation is not likely to change its sign, we can assume that the zero regions in $\hat{\boldsymbol{x}}$ and $\hat{\boldsymbol{x}}^*$ are the same. Subtracting (6) from (5) for all $j : \hat{x}_j > 0$, we get

$$\sum_k \frac{p(i_k,j)}{\sum_l p(i_k,l)\hat{x}_l^*} - \sum_k \frac{p(i_k,j)}{\sum_l p(i_k,l)\hat{x}_l} - \beta\frac{\partial}{\partial x_j}U(\hat{\boldsymbol{x}}^*) + \beta\frac{\partial}{\partial x_j}U(\hat{\boldsymbol{x}}) - \delta\varepsilon_j = 0, \quad j : \hat{x}_j > 0 \tag{7}$$

Assuming the difference between $\hat{\boldsymbol{x}}$ and $\hat{\boldsymbol{x}}^*$ is small, we use the following first order Taylor series approximations [11]

$$\sum_k \frac{p(i_k,j)}{\sum_l p(i_k,l)\hat{x}_l^*} - \sum_k \frac{p(i_k,j)}{\sum_l p(i_k,l)\hat{x}_l} \approx -\sum_k \sum_m \frac{p(i_k,j)p(i_k,m)}{\left[\sum_l p(i_k,l)\hat{x}_l\right]^2}(\hat{x}_m^* - \hat{x}_m) \tag{8}$$

$$\beta\frac{\partial}{\partial x_j}U(\hat{\boldsymbol{x}}^*) - \beta\frac{\partial}{\partial x_j}U(\hat{\boldsymbol{x}}) \approx \sum_m \frac{\partial^2}{\partial x_j \partial x_m}U(\hat{\boldsymbol{x}})(\hat{x}_m^* - \hat{x}_m) \tag{9}$$

Substituting (8) and (9) into (7) and solving the equation, we get the reconstruction error introduced by $\delta\varepsilon$

$$\delta\hat{\boldsymbol{x}} \equiv \hat{\boldsymbol{x}}^* - \hat{\boldsymbol{x}} \approx \left[\nabla^2 L(\hat{\boldsymbol{x}}) - \beta\nabla^2 U(\hat{\boldsymbol{x}})\right]^{-1}\delta\boldsymbol{\varepsilon}, \tag{10}$$

where the (j,m)th element of $\nabla^2 L(\hat{\boldsymbol{x}})$ is $-\sum_k \frac{p(i_k,j)p(i_k,m)}{\left[\sum_l p(i_k,l)\hat{x}_l\right]^2}$ and the (j,m)th element of $\nabla^2 U(\hat{\boldsymbol{x}})$ is $\frac{\partial^2}{\partial x_j \partial x_m}U(\hat{\boldsymbol{x}})$. For the quadratic prior in (3), $\nabla^2 U(\hat{\boldsymbol{x}}) = \boldsymbol{R}$. Note that the rows and columns that correspond to $\hat{x}_j = 0$ are eliminated from $\nabla^2 L(\hat{\boldsymbol{x}})$ and $\nabla^2 U(\hat{\boldsymbol{x}})$ in (10).

Equation (10) shows that the error in the sensitivity image will be amplified by $\left[\nabla^2 L(\hat{\boldsymbol{x}}) - \nabla^2 U(\hat{\boldsymbol{x}})\right]^{-1}$ in the reconstructed image. This is counter to the intuitive thinking that $\hat{x}_j^* = \hat{x}_j\varepsilon_j^*/\varepsilon_j$. For emission data, $\nabla^2 L(\hat{\boldsymbol{x}})$ is similar to the $1/r^2$ response in 3D, when ignoring the spatially variant response of the tomography system. Thus, errors of different frequency in the sensitivity image may be amplified differently depending on the prior function. Strong priors generally reduce the error propagation.

III. Computer Simulations

Computer simulations have been conducted to validate the theoretical result. We simulated a small rectangular PET scanner with 32 detectors on each side (Fig. 1a). The field of view is the whole area enclosed by the detectors represented by 32×32 square pixels. The phantom image is a uniform disk. The simulation models the solid angle effect, crystal penetration, and object attenuation. A noise free reconstruction is shown in Fig. 1b.

Figures 2 and 3 show the changes in the reconstructed images when we perturb the sensitivity image at only one pixel location. In each case, we decrease the sensitivity by 10%, which results in a local increase in reconstructed activity. As shown in both

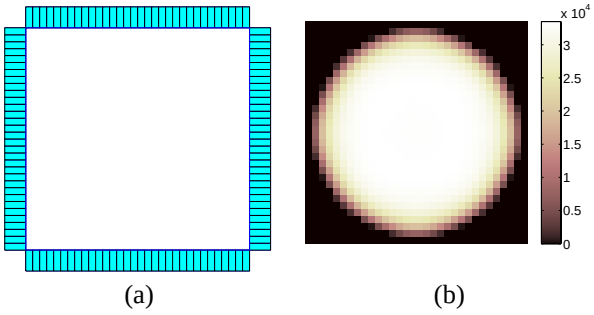

Fig. 1. Simulated rectangular scanner (a) and the reconstruction of a disk phantom (b).

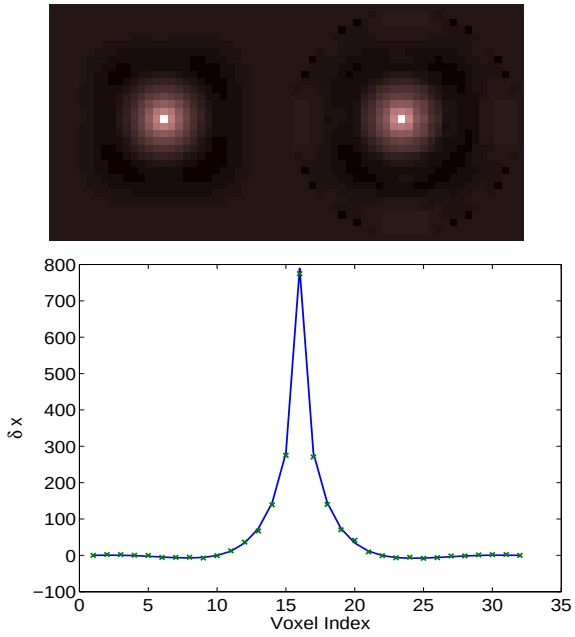

Fig. 2. Comparison of the measured error image and the theoretical prediction with a 10% perturbation at the center location. Top left: theoretical error image; top right: measured error image; bottom: vertical profiles through center of the theoretical (solid line) and the measured ('×') image.

figures, the theoretical predictions match the measured results very well.

To demonstrate the frequency-dependent amplification, we independently add three colored Gaussian noise realizations (Fig. 4) to the sensitivity image. The standard deviation of the Gaussian noise is 1% of the average sensitivity within the disk region. Figs. 5-7 show the theoretical predicted error image with comparison to the measured results for MAP reconstruction with $\beta = 1\times10^{-6}$, 1×10^{-7} and 1×10^{-8}. The relative root mean squared errors (RMSE) in the disk region are shown in Table I. The relative RMSE is computed as

$$\text{RMSE} = \sqrt{\frac{1}{P}\sum_{j\in\text{Disk}}\left[\frac{\hat{x}_j^* - \hat{x}_j}{\hat{x}_j}\right]^2},$$

where P is the number of the pixels in the disk region. Note that in most cases, the relative error in reconstruction is much larger than the error introduced in the sensitivity image. At low resolution ($\beta = 1\times10^{-6}$), the final image is more susceptible to

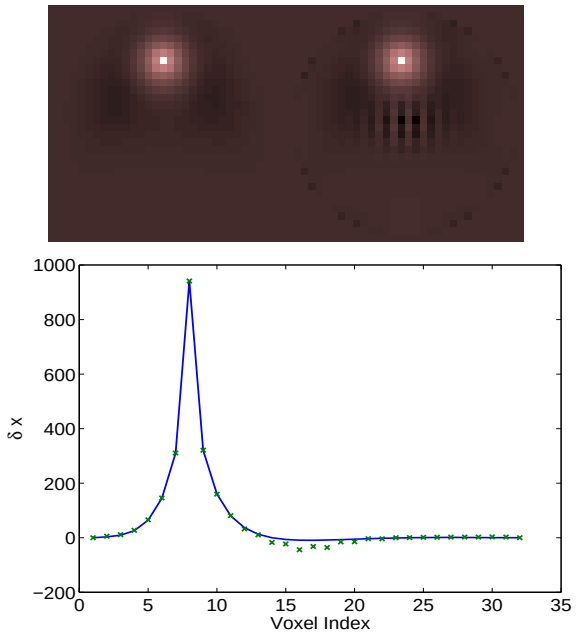

Fig. 3. Comparison of the measured error image and the theoretical prediction with a 10% perturbation at an off-center location. Top left: theoretical error image; top right: measured error image; bottom: vertical profiles through center of the theoretical (solid line) and the measured ('×') image.

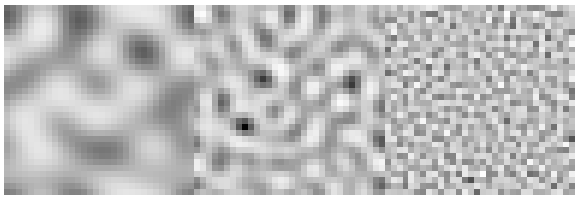

Fig. 4. The low-frequency (left), mid-frequency (center), and high-frequency (right) noise that were added to the sensitivity image.

TABLE I

THE RELATIVE ROOT MEAN SQUARED ERRORS OF THE MAP RECONSTRUCTION RESULTING FROM DIFFERENT FREQUENCY ERROR IN THE SENSITIVITY IMAGE.

β	low-freq	mid-freq	high-freq
1×10^{-6}	1.41%	0.63%	0.21%
1×10^{-7}	4.28%	4.40%	1.97%
1×10^{-8}	6.38%	14.1%	13.8%

low frequency error in the sensitivity image, while at high resolution ($\beta = 1 \times 10^{-8}$), the reconstruction is more susceptible to high frequency error in the sensitivity image. Overall, the reconstruction error with $\beta = 1 \times 10^{-6}$ is much smaller than that with $\beta = 1 \times 10^{-8}$, indicating strong priors can suppress the error propagation.

IV. Conclusion and Discussion

We have theoretically analyzed the propagation of errors from the sensitivity image into the reconstructed image in list mode likelihood reconstruction. The results show that the error in the sensitivity image will be amplified by $\left[\nabla^2 L(\hat{\boldsymbol{x}}) - \nabla^2 U(\hat{\boldsymbol{x}})\right]^{-1}$ in the final reconstruction. Computer simulations show that the

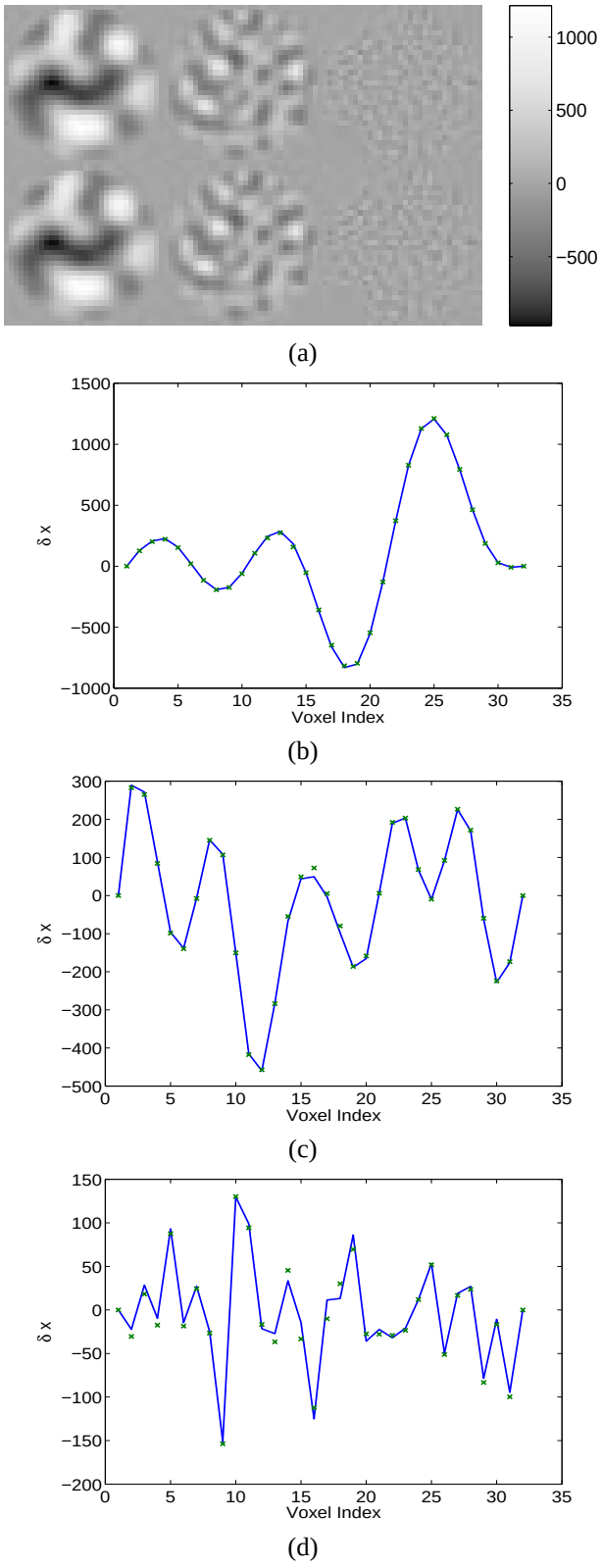

Fig. 5. Comparison of the measured error image and the theoretical prediction resulting from errors of different frequencies with $\beta = 1 \times 10^{-6}$. The error in the sensitivity image is 1% colored Gaussian noise. (a) the error images: top row: measured; bottom: theoretical. Left column: low frequency error; center column: mid frequency error; right column: high frequency error. (b) vertical profiles of low frequency error. (c) vertical profiles of mid frequency error. (d) vertical profiles of high frequency error. The legends are theoretical predictions (solid lines) and measured results ('×').

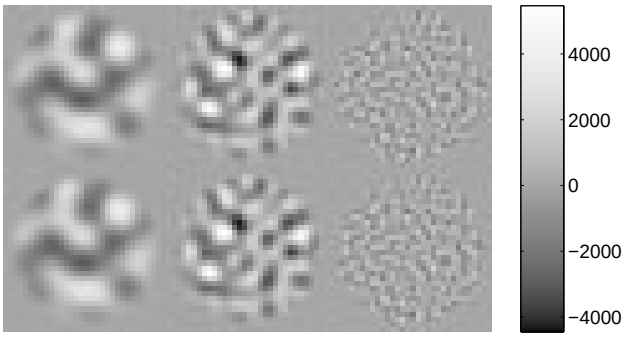

(a)

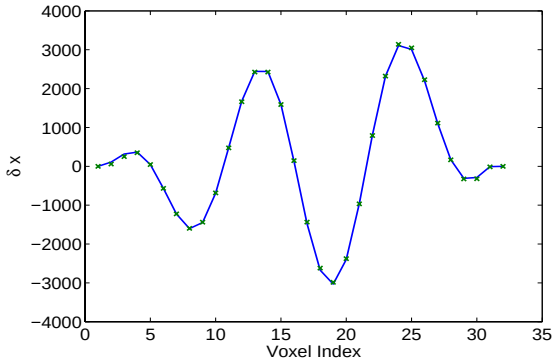

(b)

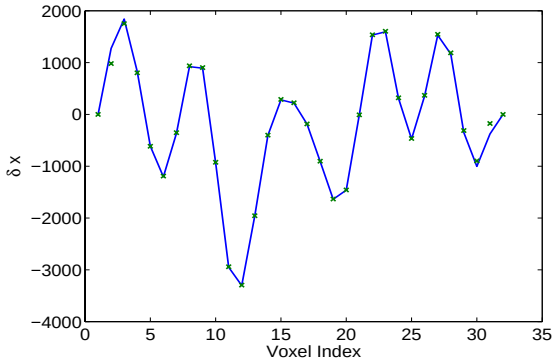

(c)

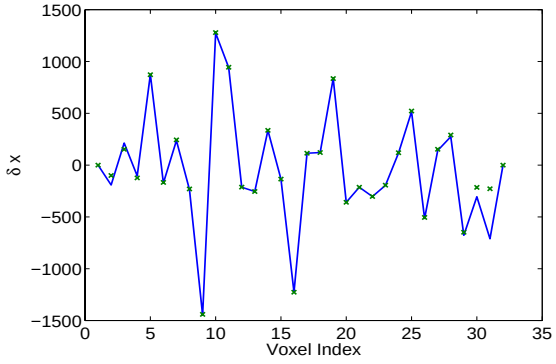

(d)

Fig. 6. Comparison of the measured error image and the theoretical prediction resulting from errors of different frequencies with $\beta = 1 \times 10^{-7}$. The error in the sensitivity image is 1% colored Gaussian noise. (a) the error images: top row: measured; bottom: theoretical. Left column: low frequency error; center column: mid frequency error; right column: high frequency error. (b) vertical profiles of low frequency error. (c) vertical profiles of mid frequency error. (d) vertical profiles of high frequency error. The legends are theoretical predictions (solid lines) and measured results ('×').

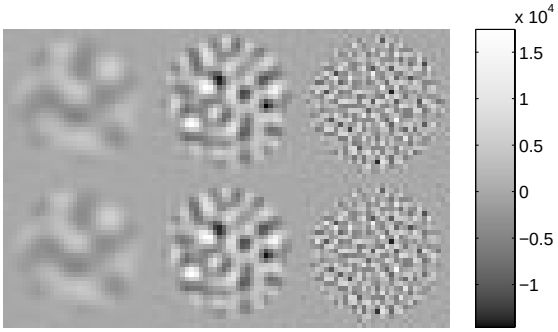

(a)

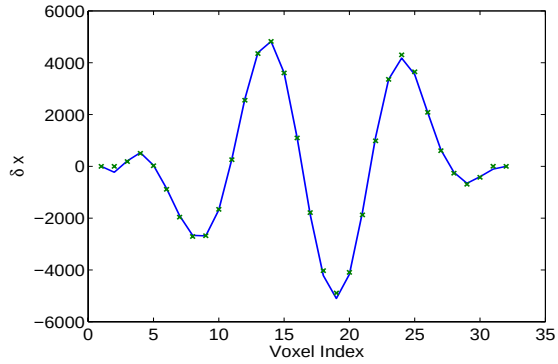

(b)

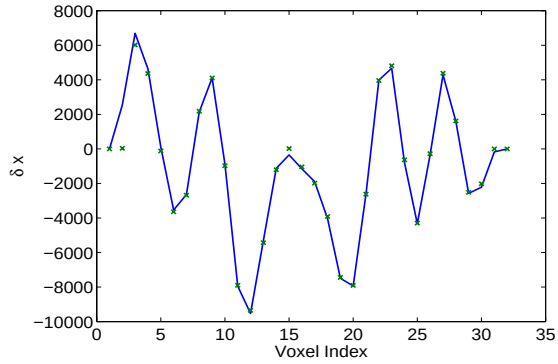

(c)

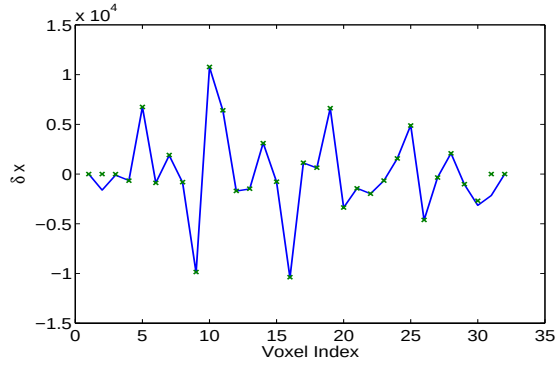

(d)

Fig. 7. Comparison of the measured error image and the theoretical prediction resulting from errors of different frequencies with $\beta = 1 \times 10^{-8}$. The error in the sensitivity image is 1% colored Gaussian noise. (a) the error images: top row: measured; bottom: theoretical. Left column: low frequency error; center column: mid frequency error; right column: high frequency error. (b) vertical profiles of low frequency error. (c) vertical profiles of mid frequency error. (d) vertical profiles of high frequency error. The legends are theoretical predictions (solid lines) and measured results ('×').

theoretical predictions match the measured results very well.

The theoretical expression is useful for analyzing list mode reconstruction and for developing fast approaches to compute the sensitivity image. Since the error amplification is resolution dependent, different reconstruction may require different approximation of the sensitivity image. In practice, we need first to determine the expected resolution in reconstruction, then use the theoretical expression (10) to find the sensitive region in the frequency domain and try to reduce the error in the sensitive frequency range from the sensitivity image.

REFERENCES

[1] L. Parra and H. H. Barrett, "List-mode likelihood: EM algorithm and image quality estimation demonstrated on 2-D PET," *IEEE Transactions on Medical Imaging*, pp. 228–235, 1998.

[2] R. H. Huesman, G. J. Klein, W. W. Moses, J. Qi, B. W. Reutter, and P. R. G. Virador, "List mode maximum likelihood reconstruction applied to positron emission mammography with irregular sampling," *IEEE Transactions on Medical Imaging*, vol. 19, pp. 532–537, 2000.

[3] C. Byrne, "Likelihood maximization for list-mode emission tomographic image reconstruction," *IEEE Transactions on Medical Imaging*, vol. 20, pp. 1084–1092, 2001.

[4] A. J. Reader, K. Erlandsson, M. A. Flower, and R. J. Ott, "Fast accurate iterative reconstruction for low-statistics positron volume imaging," *Physics in Medicine and Biology*, vol. 43, pp. 835–846, 1998.

[5] R. Levkovilz, D. Falikman, M. Zibulevsky, A. Ben-Tal, and A. Nemirovski, "The design and implementation of COSEM, an iterative algorithm for fully 3-D listmode data," *IEEE Transactions on Medical Imaging*, vol. 20, pp. 633–642, 2001.

[6] A. Reader, S. Ally, F. Bakatselos, R. Manavaki, R. Walledge, A. Jeavons, P. Julyan, Z. Sha, D. Hastings, and J. Zweit, "One-pass list-mode EM algorithm for high-resolution 3-D PET image reconstruction into large arrays," *IEEE Transactions on Nuclear Science*, vol. 49, pp. 693–699, 2002.

[7] M. Schmand, K. Wienhard, M. Casey, L. Eriksson, W. F. Jones, J. H. Reed, J. Treffert, M. Lenox, P. Luk, J. Bao, J. W. Young, K. Baker, S. D. Miller, C. Knoess, S. Vollmar, N. Richerzhagen, G. Flugge, W. D. Heiss, and R. Nutt, "Performance evaluation of a new LSO high resolution research tomograph - HRRT," in *Proceedings of IEEE Nuclear Science Symposium and Medical Imaging Conference*, pp. 1067–1071, Seattle, WA, 1999.

[8] J. Qi and R. H. Huesman, "List mode reconstruction for PET with motion compensation: A simulation study," in *Proceedings of IEEE International Symposimum on Biomedical Imaging*, pp. 413–416, 2002.

[9] R. E. Carson, W. C. Barker, J. S. Liow, S. adler, and C. A. Johnson, "Design of a motion-compensation OSEM list-mode algorithm for resolution-recovery reconstruction for the HRRT," in *Proceedings of IEEE Nuclear Science Symposium and Medical Imaging Conference*, pp. M16–6, 2003.

[10] D. Luenberger, *Linear and Nonlinear Programming*, Addison-Wesley Publishing Company, second edition, 1984.

[11] J. Fessler, "Mean and variance of implicitely defined biased estimators (such as penalized maximum likelihood): Applications to tomography," *IEEE Transactions on Image Processing*, vol. 5, pp. 493–506, 1996.